

COOL-CORE CLUSTERS : ROLE OF BCG, STAR FORMATION & AGN-DRIVEN TURBULENCE

DEOVRAT PRASAD¹ AND PRATEEK SHARMA¹

¹Joint Astronomy Program and Department of Physics, Indian Institute of Science, Bangalore, India 560012

ARIF BABUL²

²Department of Physics and Astronomy, University of Victoria, Victoria, BC V8P 1A1, Canada

Draft version March 8, 2024

ABSTRACT

Recent analysis shows that it is important to explicitly include the gravitational potential of the central brightest central galaxy (BCG) to infer the acceleration due to gravity (g) and the free-fall time ($t_{\text{ff}} \equiv [2r/g]^{1/2}$) in cool cluster cores. Accurately measuring t_{ff} is crucial because according to numerical simulations cold gas condensation and strong feedback occur in cluster cores with $\min(t_{\text{cool}}/t_{\text{ff}})$ below a threshold value close to 10. Recent observations which include the BCG gravity show that the observed threshold in $\min(t_{\text{cool}}/t_{\text{ff}})$ lies at a somewhat higher value, close to 10-30; there are only a few clusters in which this ratio falls much below 10. In this paper we compare numerical simulations of feedback AGN (Active Galactic Nuclei) jets interacting with the intracluster medium (ICM), with and without a BCG potential. We find that, for a fixed feedback efficiency, the presence of a BCG does not significantly affect the temperature but increases (decreases) the core density (entropy) on average. Most importantly, $\min(t_{\text{cool}}/t_{\text{ff}})$ is only affected slightly by the inclusion of the BCG gravity. Also notable is that the lowest value of $\min(t_{\text{cool}}/t_{\text{ff}})$ in the NFW+BCG runs are about twice larger than in the NFW runs because of a shorter time for feedback heating (which scales with the free-fall time) in the former. We also look at the role of depletion of cold gas due to star formation and show that it only affects the rotationally dominant component (torus), while the radially dominant component (which regulates the feedback cycle) remains largely unaffected. Stellar gas depletion also increases the duty cycle of AGN jets. The distribution of metals due to AGN jets in our simulations is predominantly along the jet direction and the radial spread of metals is less compared to the observations. We also show that the turbulence in cool core clusters is weak, consistent with recent *Hitomi* results on Perseus cluster.

Subject headings: galaxies: clusters: intra-cluster medium – galaxies: halos – galaxies: jets

1. INTRODUCTION

Dense X-ray emitting plasma in cool cluster cores is susceptible to thermal fragmentation, leading to the formation of a multiphase medium consisting of cold dense clouds condensing from the hot ICM. The infall and accretion of these cold clouds onto the central super massive black hole (SMBH) powers the AGN outbursts that maintain the ICM (Pizzolato & Soker 2005) in rough thermal balance. Early idealized simulations predicted that cold gas stochastically condenses out of the hot ICM if the minimum in the ratio of the cooling time to the free-fall time ($\min[t_{\text{cool}}/t_{\text{ff}}]$) falls below a threshold close to 10 (McCourt et al. 2012; Sharma et al. 2012). This cold gas is expected to lose angular momentum due to cloud-cloud collisions and due to drag imparted by the hot gas, fall inwards and fuel AGN outbursts (Gaspari et al. 2013; Prasad et al. 2016). The feedback process is self-regulatory with phases dominated by radiative cooling and jet heating (McNamara et al. 2005; Rafferty et al. 2006). Several recent feedback jet simulations evolved over cosmological timescales are now able to reproduce the gross observed properties of cool cluster cores (Gaspari et al. 2012; Li et al. 2015; Prasad et al. 2015; Yang

& Reynolds 2016b).

Since AGN feedback is triggered by the precipitation of cold gas from the hot ICM (Sharma et al. 2012; Voit et al. 2015), the feedback process is sensitively dependent on the properties of X-ray emitting gas in cluster cores. Recent works like Voit & Donahue (2015); Hogan et al. (2017a,b) highlight the importance of explicitly including the central brightest cluster galaxy (BCG) to determine the acceleration due to gravity (g) and free-fall time ($t_{\text{ff}} \equiv [2r/g]^{1/2}$) in cluster cores. Most cool core clusters have BCGs at their centers whose gravity dominates the gravity due to the dark matter halo within the central 20-30 kpc. Hogan et al. (2017b) argue that including the BCG gravity increases $\min(t_{\text{cool}}/t_{\text{ff}})$ in most cool core clusters above 10, and hence observations are in tension with the simulation results that find $\min(t_{\text{cool}}/t_{\text{ff}})$ drop down to a few (albeit for a short time). In this paper we test if including the BCG potential changes the value of $\min(t_{\text{cool}}/t_{\text{ff}})$ in the jet-ICM simulations, and compare our simulation results with observations.

The AGN-ICM coupling can happen through shocks (Fabian et al. 2003; Li et al. 2016), turbulence (Zhuravleva et al. 2014), mixing (Banerjee & Sharma 2014; Hillel & Soker 2016), entrainment (McNamara et al. 2005; Pope et al. 2010), cosmic rays and thermal conduction (Voigt & Fabian 2004; Guo & Oh 2008; Sharma et al. 2009a) or a combination of these processes (Cielo et al. 2018). How-

ever, the relative importance of these various processes in heating the cluster core is not clear. Among these mechanisms, turbulent heating seems to be ruled out by recent *Hitomi* observations of the Perseus cluster (Hitomi Collaboration et al. 2016), which show that the turbulence level in the cluster core is weak. Even if turbulent heating may not be the dominant mechanism for core heating, turbulent mixing and diffusion still plays an important role in core thermodynamics and in transporting out the freshly created metals in star-forming cool cluster cores. Consequently another aim of our paper is to compare AGN-driven turbulence in our simulations with the observational constraints on ICM turbulence.

In addition to maintaining rough thermal equilibrium in cool core clusters, AGN jets, as they rise buoyantly to 100s of kpc, also play a potential role in distributing metals by entraining metal enriched gas (Pope et al. 2010; Revaz et al. 2008) from star forming inner regions of the cool-core clusters. Observations show that in nearby cool core clusters the central ~ 100 kpc have a sharply rising metallicity while the outer regions have a constant metallicity (Tamura et al. 2004; Fujita et al. 2008; Simionescu et al. 2011; Werner et al. 2013). On the other hand, in non-cool clusters the metallicity in the cluster core increases only marginally with a decreasing radius, with the outer regions having a fixed metallicity similar to cool-core clusters (Leccardi & Molendi 2008). Further, the metallicity within the central 100-150 kpc evolves with redshift ($z < 1.4$) in cool core clusters while the outer regions do not show any evolution (Ettori et al. 2015).

Observations of several cool core clusters show that the metallicity is high beyond the cluster core along the AGN jet direction (Simionescu et al. 2009; Kirkpatrick et al. 2009; O’Sullivan et al. 2011) as compared to the perpendicular direction. This suggests that the cavities created by AGN jets are able to carry the metal enriched gas to regions beyond the star forming cluster cores. Further, as the AGN outflow is bi-conical in nature, the isotropic distribution of metals (at a rather large value $\approx 0.3Z_{\odot}$) in cluster outskirts suggests that the metal enrichment of ICM out to the virial radius happened at early times, by when most of the metals in the universe were already produced. We include a crude model for metal injection by injecting metallicity within small biconical jet source regions rather than following the stellar distribution in the BCG. Metallicity at ~ 100 kpc should be affected mainly by transport due to AGN jets rather than by injection. Moreover, we only consider metal production in the cluster center and ignore the dominant process of early enrichment in which metals were produced far from the BCG within the galaxies that merged to form the eventual cluster. The aim of our metallicity study is limited – to quantify the dispersal of metals only due to AGN jets in realistic cool cores.

This paper is organized as follows. In section 2 we present the numerical setup followed by analysis methods. Section 3 presents the key results of our 3-D simulations. We compare the simulations with and without the central BCG in detail. We provide a quantitative comparison between the BCG+NFW runs with and without stellar depletion. We also analyze hot gas velocity distribution and turbulence in cluster cores, and discuss the nature of metal distribution due to AGN jets. In section

4 we compare our results with observations and discuss their implications. We conclude with a brief summary in section 5.

2. NUMERICAL SETUP

We modified the PLUTO MHD code (Mignone et al. 2007) to simulate AGN feedback in galaxy clusters. We solve the standard hydrodynamic equations in spherical coordinates (r, θ, ϕ) with cooling, external gravity and mass and momentum source terms due to AGN jet feedback, as described in section 2 of Prasad et al. (2015). We explore the effects of BCG at the centre of galaxy cluster by including the BCG potential along with the usual NFW potential. We use the same feedback prescription as Prasad et al. (2015), with a fixed feedback efficiency, $\epsilon = \dot{M}_j v_j^2 / \dot{M}_{\text{acc}} c^2 = 5 \times 10^{-4}$ (see Eq. 6 in Prasad et al. 2015), where \dot{M}_j is the jet mass loading rate, v_j ($= 0.1c$, c is the speed of light) is the injected jet velocity, and \dot{M}_{acc} is the accretion rate through the radial inner boundary of the domain at $r_{\text{in}} = 0.5$ kpc. These parameters are somewhat different from our previous papers (Prasad et al. 2015, 2016) but our results are qualitatively similar.

2.1. Gravitational Potential

The dark matter halo mass (M_{200}) for all our runs is $7 \times 10^{14} M_{\odot}$. One of our runs uses only the NFW gravitational potential (Navarro et al. 1997). For the other two runs the external gravitational potential is the sum of two different potentials: 1) NFW dark matter potential, and 2) a singular isothermal sphere (SIS) for the central brightest cluster galaxy,

$$\Phi = \Phi_{\text{NFW}} + \Phi_{\text{SIS}}. \quad (1)$$

The singular isothermal sphere potential (SIS) for the brightest cluster galaxy is given by:

$$\Phi_{\text{SIS}}(r) = 4\pi G \rho_0 a_0^2 \ln(r/a_0), \quad (2)$$

where $\rho_0 = 1.67 \times 10^{-23} \text{ g cm}^{-3}$ and $a_0 = 3$ kpc. The isothermal sphere circular velocity $V_c = \sqrt{4\pi G \rho_0 a_0^2} = 350 \text{ km s}^{-1}$. The circular velocity is in the range of V_c observed in the cluster sample of Hogan et al. (2017a) (note that this paper uses the equivalent stellar velocity dispersion $\sigma_{\star} = V_c/\sqrt{2}$).

2.2. Grid, Initial and Boundary Conditions

We perform our simulations in spherical coordinates with $0 \leq \theta \leq \pi$, $0 \leq \phi \leq 2\pi$, and $r_{\text{min}} \leq r \leq r_{\text{max}}$, with $r_{\text{min}} = 0.5$ kpc and $r_{\text{max}} = 500$ kpc. We use a logarithmically spaced grid in radius, and an equally spaced grid in θ and ϕ .

The outer electron number density is fixed to be $n_e = 7 \times 10^{-4} \text{ cm}^{-3}$. Given the entropy profile with a core (Eq. 7 in Prasad et al. 2015) and the outer density, we solve for hydrostatic equilibrium and obtain the density and pressure profiles in the gravitational potential (for details see Prasad et al. 2015). As in Prasad et al. (2015), we introduce small (maximum over-density is 0.3) isobaric density perturbations on top of the smooth density. The gas is allowed to cool to 50 K unlike Prasad et al. (2015) where cooling was cut-off at 10^4 K.

We apply outflow boundary conditions at the inner radial boundary, where gas is allowed to go out of the computational domain but not allowed to enter it. We fix the density and pressure at the outer radial boundary to the initial value and the gas is not allowed to flow in/out of the outer radial boundary. Reflective boundary conditions are applied in θ (with the sign of v_ϕ flipped at the poles) and periodic boundary conditions are used in ϕ .

2.3. Stellar Gas Depletion

One of our runs (see Table 1) implements a crude model for mass depletion of cold gas due to star formation. To simulate the removal of cold gas due to star formation, we deplete the cold gas with temperature $T < 0.005$ keV ($\approx 5 \times 10^4$ K) and density $\rho > 10^{-24}$ g cm $^{-3}$ using a sink term in the mass conservation equation

$$\frac{\partial \rho}{\partial t} + \nabla \cdot (\rho \mathbf{v}) = S_\rho - D_\rho, \quad (3)$$

where the depletion term $D_\rho = \rho/\tau$ and $\tau = 200$ Myr is the gas depletion timescale (this is on the lower side of the range seen in observations; e.g., see Fig. 9 of Pulido et al. 2018). Note that there is a large uncertainty in the determination of the star formation rate and hence τ (e.g., see Mittal et al. 2015). Our choice of τ is such that our cold gas mass is in a range consistent with observations. Here, S_ρ is the usual AGN jet mass source term as in Eq. 1 of Prasad et al. (2015). Note that, unlike here, in Prasad et al. (2016) we only accounted for stellar depletion in post processing. We do not consider feedback due to star formation because it is sub-dominant compared to AGN feedback in massive halos.

2.4. Metallicity

Using our realistic cool core simulations, we also wish to study the jet-driven transport of metals produced recently (after majority of stars within the cluster have already formed and the cluster with a cool core is assembled) in the BCGs of cool-core clusters. To quantify the spread of metals in the ICM, we evolve the passive scalar equation with a source term in the jet mass source region

$$\frac{\partial Z}{\partial t} + \mathbf{v} \cdot \nabla Z = Z_j \frac{S_\rho}{\rho}, \quad (4)$$

where Z is the metallicity defined as the ratio of metal mass and total gas mass (normalized to the solar value, Z_\odot), Z_j is the normalization of the jet metallicity and S_ρ is the jet mass source term (see Eq. 3). The jet metallicity Z_j is somewhat arbitrary as our focus is on the spatial spread of metals due to AGN jets rather than the actual value of metallicity. We choose $Z_j = 100$ as it gives a reasonable metallicity values for the simulated ICM. This value is also justified by considering the mass loading factor of AGN jets relative to the star formation rate in the BCG. From our jet feedback prescription, $\dot{M}_j = (\epsilon c^2/v_j^2)\dot{M}_{\text{acc}} = 0.05\dot{M}_{\text{acc}}$ for our parameters.¹ The mass accretion rate at 0.5 kpc is $\sim 5M_\odot \text{ yr}^{-1}$

¹ As emphasized in Prasad et al. (2016), \dot{M}_{acc} depends on the choice of r_{in} . Current cluster simulations simply do not have the resolution to directly simulate accretion on to the SMBH.

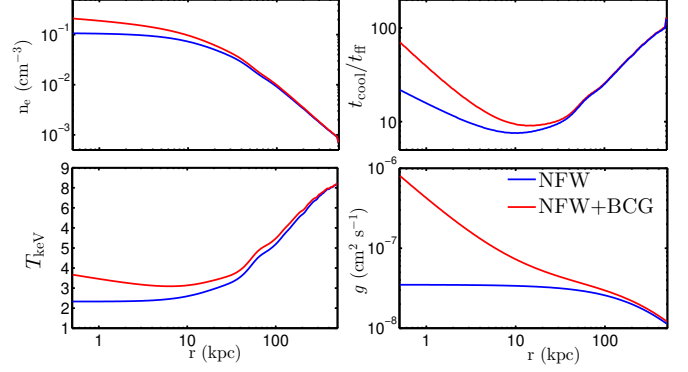


FIG. 1.— Comparison of the initial electron number density, temperature, $t_{\text{cool}}/t_{\text{ff}}$ and gravitational acceleration (g) profiles for the NFW (blue line) and NFW+BCG (red line) runs. The effect of the BCG is felt only within the central 50 kpc.

(see Table 1). On the other hand the average star formation rate (SFR) is expected to be a few 10s of $M_\odot \text{ yr}^{-1}$. Since all the metals produced due to star formation in the BCG are deposited in the jet region in our simulations, $Z_j \sim (\text{SFR}/\dot{M}_{\text{acc}}) \times (\dot{M}_{\text{acc}}/\dot{M}_j) \approx 5 \times 20 = 100$ is a reasonable order of magnitude normalization for the metal source term.

In our metallicity profiles (c.f. Figs. 9 & 10) we add $0.3Z_\odot$ to account for the ambient metallicity close to the viral radius due to early enrichment. The radial spread of metals due to AGN jets is quantified using,

$$Z(r) = \frac{\int_\theta \int_\phi Z(r, \theta, \phi) \rho \sin \theta d\theta d\phi}{\int_\theta \int_\phi \rho \sin \theta d\theta d\phi}, \quad (5)$$

where r is the radius. Similarly, the angular distribution of metallicity due to AGN jets is quantified by

$$Z(\theta) = \frac{\int_r \int_\phi Z(r, \theta, \phi) \rho r \sin \theta dr d\phi}{\int_r \int_\phi \rho r \sin \theta dr d\phi}. \quad (6)$$

3. RESULTS

In this section we describe the important results of our simulations. Table 1 lists all our runs. We show that the inclusion of BCG potential does not affect the cluster temperature but affects the average electron number density, $t_{\text{cool}}/t_{\text{ff}}$ and entropy profiles in the core. We study the effect of stellar cold gas depletion on cluster evolution. We also show that the turbulence level in cluster cores is weak, consistent with the recent *Hitomi* results. We find that the metal distribution is anisotropic and too narrow in radius as compared to the observations.

3.1. NFW vs NFW+BCG potential

3.1.1. Average 1-D Profiles

Figure 1 shows the initial angle-averaged profiles of electron number density, temperature, $t_{\text{cool}}/t_{\text{ff}}$ and gravitational acceleration (g) for the runs with NFW and NFW+BCG potentials. The plots show that the effect of BCG is felt only within the central 50 kpc of the cluster. The density and temperature in the core are nearly double when the BCG potential is included. Bottom right panel of Figure 1 shows that the inclusion of BCG potential makes the gravitational acceleration rise sharply at small radii. This affects the $t_{\text{cool}}/t_{\text{ff}}$ profile in the inner

TABLE 1
LIST OF RUNS

Run	r_{in} (kpc)	r_{out} (kpc)	ϵ	run time (Gyr)	\dot{M}_{acc} ($M_{\odot}\text{yr}^{-1}$)	M_{cold} ($10^{10} M_{\odot}$)	τ (Myr)	fraction of time for which $\min(t_{\text{cool}}/t_{\text{ff}}) < 10, 5$
NFW	0.5	500	5×10^{-4}	4	4.4	2.0	∞	47%, 14%
NFW+BCG	0.5	500	5×10^{-4}	4	6.7	4	∞	55%, 14%
NFW+BCGd [†]	0.5	500	5×10^{-4}	4	7.1	0.2	200	77%, 19%

The M_{200} for all the runs is $7 \times 10^{14} M_{\odot}$. The resolution of all runs, done in spherical ($r_{\text{min}} \leq r \leq r_{\text{max}}, 0 \leq \theta \leq \pi, 0 \leq \phi \leq 2\pi$) coordinates, is $256 \times 128 \times 32$. A logarithmic grid is used in the r – direction, and a uniform one in others. \dot{M}_{acc} is the average (cold+hot) mass accretion rate across r_{in} from 0 to 4 Gyr; M_{cold} is the total cold ($T < 0.005$ keV) gas mass in the simulation domain by the end of the run.

[†] ‘d’ at the end of the label stands for depletion of cold gas.

regions ($r \lesssim 20$ kpc). The BCG potential, as we discuss later, also shortens the feedback response time and prevents $\min(t_{\text{cool}}/t_{\text{ff}})$ in NFW+BCG runs from falling below ≈ 2 . The initial $\min(t_{\text{cool}}/t_{\text{ff}})$ is 8.8 for the NFW run while it is 9.8 for the NFW+BCG run.

Figure 2 shows the mean and $1 - \sigma$ spread in the angle-averaged, emissivity weighted electron number density, temperature, entropy and $t_{\text{cool}}/t_{\text{ff}}$ profiles for the X-ray emitting gas (0.5–10 keV) from 1–4 Gyr for NFW and NFW+BCG runs. The mean and 1σ spread about the mean are calculated at each radius for different quantities between 1–4 Gyr. The density plot in Figure 2 shows that the average core density and the 1σ spread about the mean are higher for the NFW+BCG run as compared to the NFW run. This higher electron number density is expected as the deeper potential well makes it difficult for AGN jets to remove the gas from the cluster core (due to the addition of the BCG potential).

Unlike density, temperature does not show any significant difference for the NFW and NFW+BCG runs. Although, there was a difference in the initial cluster core temperature (see Figure 1), radiative cooling and AGN heating cycles remove this difference during the course of long term evolution. As a result of electron number density being higher for the NFW+BCG run, entropy ($K = T_{\text{keV}}/n_e^{2/3}$) is correspondingly lower. The 1σ spread of entropy about the mean has a small overlap in the cluster core while they almost lie on top of each other at larger radii. This shows that the effect of BCG is only felt within the central 50 kpc of the cluster. Outer regions are largely unaffected by the presence of BCG at the cluster centre.

The evolution of $t_{\text{cool}}/t_{\text{ff}}$ profile in Figure 2 shows a behavior similar to entropy for both NFW and NFW+BCG runs. Similar to entropy, the average $t_{\text{cool}}/t_{\text{ff}}$ profile separates below 50 kpc for the NFW and NFW+BCG runs. Owing to a shallower potential well, AGN jets are able to evacuate the core in the NFW run easily, leading to a longer cooling time. Despite having a longer free-fall time (t_{ff}), the longer cooling time (t_{cool}) leads to a $t_{\text{cool}}/t_{\text{ff}}$ ratio for the NFW run which is above that of the NFW+BCG run with small overlap in the core. For a shallower potential well, AGN jets are able to cause overheating out to larger distances from the centre.

3.1.2. Jet Power and X-ray Luminosity

One of the ways to look at cooling and heating in clusters is to compare the core X-ray luminosity (a crude

measure of cooling) and jet/cavity power (a crude measure of heating). Figure 3 shows the variation of cavity power (P_{cav}), a proxy for jet power, with the core ($r < 30$ kpc) X-ray luminosity of gas between 0.5 to 2 keV (L_{x}) for the runs with and without the BCG potential. Cavity power is calculated as described in section 3.1.5 of Prasad et al. (2015). Most of the points lie above the $P_{\text{cav}} = L_{\text{x}}$ locus, showing that the cluster is overheated at most times for our choice of accretion efficiency in both cases. Although not apparent from this plot, P_{cav} and L_{x} show an anti-clockwise cyclic behaviour in $P_{\text{cav}} - L_{\text{x}}$ space as anticipated by Sun 2009; McDonald et al. 2010. The dense cooling cluster cores with small jet power to begin with, start accreting at a high rate after the condensation and infall of cold gas. A large jump in accretion rate leads to an increase in the jet power and overheating of the core. After a while, with a suppressed accretion rate the core cools and stage is set for another heating cycle. Further, in the NFW+BCG run, extreme heating events are absent compared to the NFW case. This is a consequence of a deeper potential well in the NFW+BCG run. Also unlike the NFW+BCG run, the NFW run spends significant time with $P_{\text{cav}} > 10^{46}$ erg s^{-1} (see also Fig. 4).

Another important point that is obvious from Figure 3 is that the correlation between the cavity power and core X-ray luminosity is rather weak, and there are hysteresis cycles (a key focus of Prasad et al. 2015). The correlation is expected to be much tighter in single phase Bondi accretion (Prasad et al. 2016). Because of the episodic nature of cold gas accretion, for the same core X-ray luminosity (or equivalently $\min(t_{\text{cool}}/t_{\text{ff}})$), very different cavity powers are seen.

3.1.3. Jet Power, $\min(t_{\text{cool}}/t_{\text{ff}})$ & Cold Gas Mass

Figure 4 shows the time evolution of jet power, cold gas mass and $\min(t_{\text{cool}}/t_{\text{ff}})$ for the NFW and NFW+BCG runs. Note that in the run with just the NFW potential (left panel), there are fewer, more powerful jet events of longer duration than in the NFW+BCG run (right panel). As the NFW potential is shallower compared to NFW+BCG potential, the jets are able to cause greater disruption. This leads to more frequent and small duration radiative cooling and AGN heating cycles for the NFW+BCG run as compared to the NFW run. In both cases, we see a rotationally dominant, stable cold gas torus forming in the central few kpc, as has been reported in several works (e.g. Gaspari et al. 2012; Li et al. 2015;

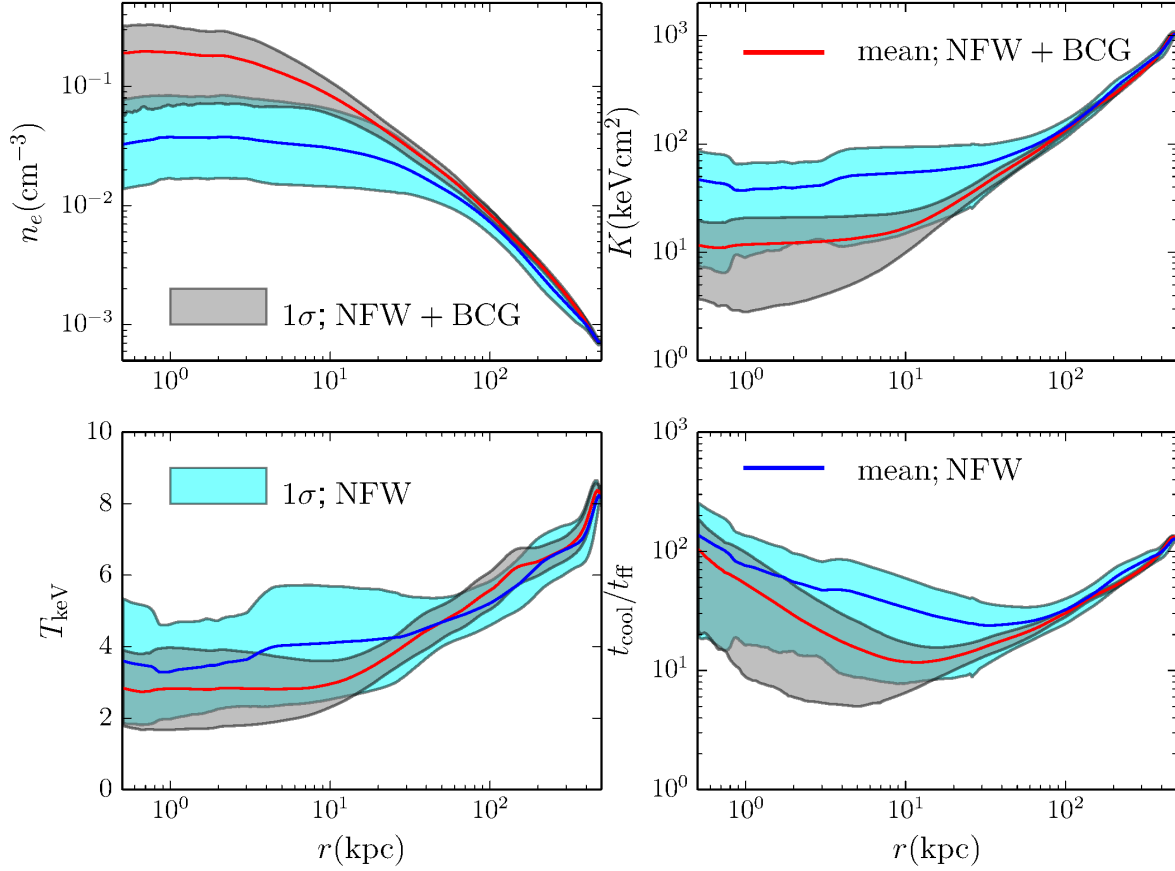


FIG. 2.— Angle-averaged, emissivity-weighted electron number density, temperature, entropy and $t_{\text{cool}}/t_{\text{ff}}$ profiles and 1σ spread at all radii calculated from the mean value for the X-ray gas (0.5–10 keV) from 1–4 Gyr. The electron number density is on the higher side for the NFW+BCG run compared to the NFW run throughout evolution but the temperature profiles are similar for both cases.

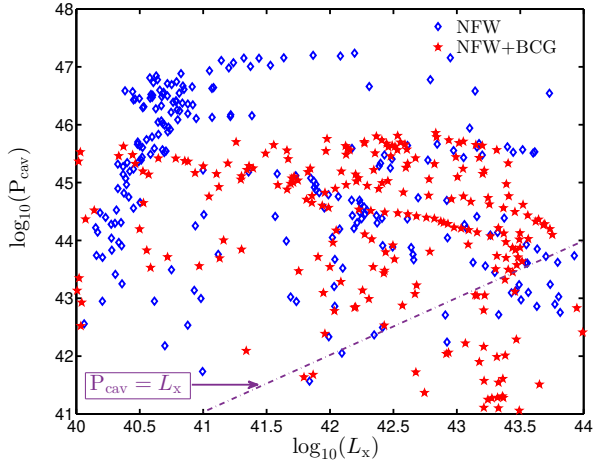


FIG. 3.— Cavity/jet power (P_{cav}) plotted against X-ray luminosity of the core ($r < 30$ kpc, L_X ; 0.5–2 keV) for the run with (stars) and without (diamonds) the BCG potential. The dot-dashed purple line shows the locus of $P_{\text{cav}} = L_X$. With most of the points lying above the $P_{\text{cav}} = L_X$ line, the clusters are over-heated at most times for the chosen feedback efficiency (ϵ).

Prasad et al. 2015). By the end of 4 Gyr the amount of cold gas exceeds $10^{10} M_{\odot}$ in both cases, with most of the

cold gas localized in the massive torus.

The NFW run shows larger $\min(t_{\text{cool}}/t_{\text{ff}})$ values after the jet events compared to the NFW+BCG run. Table 1 shows that the NFW run has $\min(t_{\text{cool}}/t_{\text{ff}})$ below 10 for 47% of the run time, while for the NFW+BCG run $\min(t_{\text{cool}}/t_{\text{ff}})$ is below 10 for a higher fraction (55%) of the time. The fraction of time spent with $\min(t_{\text{cool}}/t_{\text{ff}}) < 5$ is 14% in both cases. Therefore, we expect only a small number of clusters with $\min(t_{\text{cool}}/t_{\text{ff}}) < 5$. The range of $\min(t_{\text{cool}}/t_{\text{ff}})$ for the NFW run is 1–30 while it is 2–22 for the NFW+BCG run. Due to stronger gravity in latter, the feedback response time is shorter; consequently, $\min(t_{\text{cool}}/t_{\text{ff}})$ in NFW+BCG case never drops below 2 while in the NFW case it can drop below 1. For the same reason, jet power in the NFW+BCG run does not reach as high as in the NFW run; heating phase starts quickly before a lot of cooling (followed by large jet power) occurs. The $\min(t_{\text{cool}}/t_{\text{ff}})$ ratio and jet power are not perfectly anti-correlated. There are times when accretion of gas clouds lingering from previous cycles leads to strong jet outburst even when the core is not back to $\min(t_{\text{cool}}/t_{\text{ff}}) < 10$. At times, multiple such events can occur in quick succession, especially when $\min(t_{\text{cool}}/t_{\text{ff}})$ is close to 10.

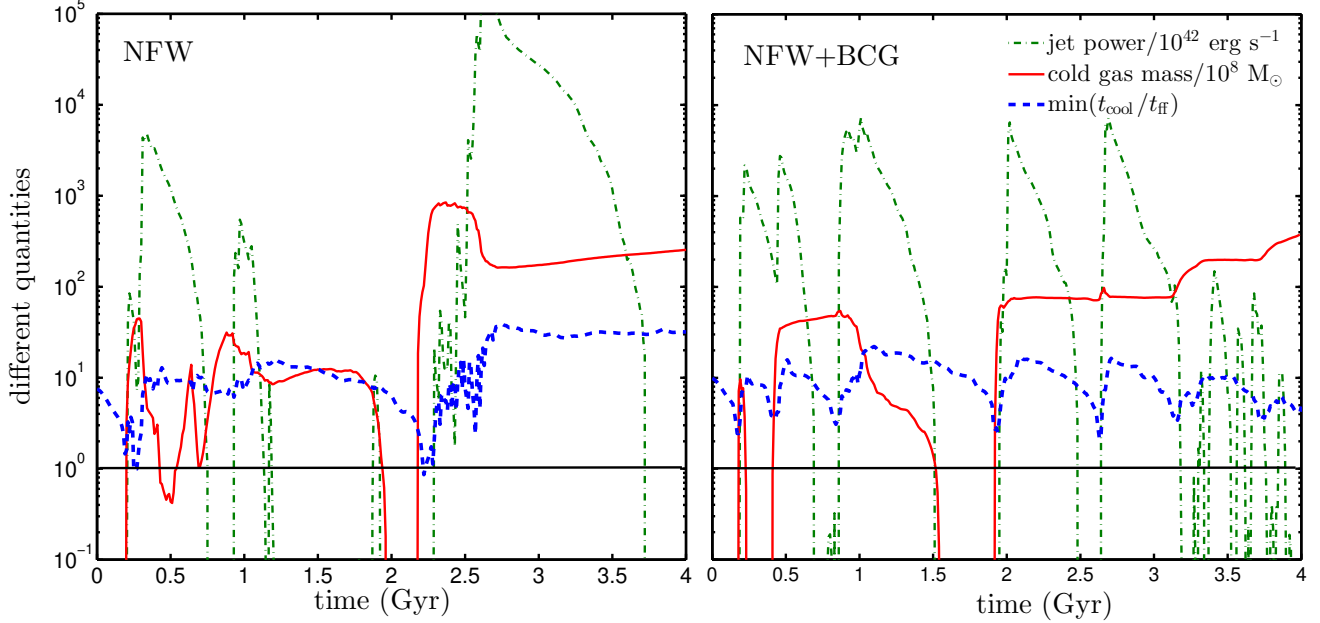


FIG. 4.— Jet power (dot-dashed green line), cold gas mass (solid red line) and $\min(t_{\text{cool}}/t_{\text{ff}})$ (blue squares) for the NFW (left panel) and the NFW+BCG (right panel) run. The time duration between consecutive jet events is different in the two cases with the NFW run having more powerful and longer jet events compared to the NFW+BCG run. The cold gas mass at the end of 4 Gyr differs in the two cases by a factor of less than 2. The AGN jets are more disruptive in the NFW run in comparison to the NFW+BCG run. While in the NFW run $\min(t_{\text{cool}}/t_{\text{ff}})$ goes below 1, for NFW+BCG it never drops below 2.

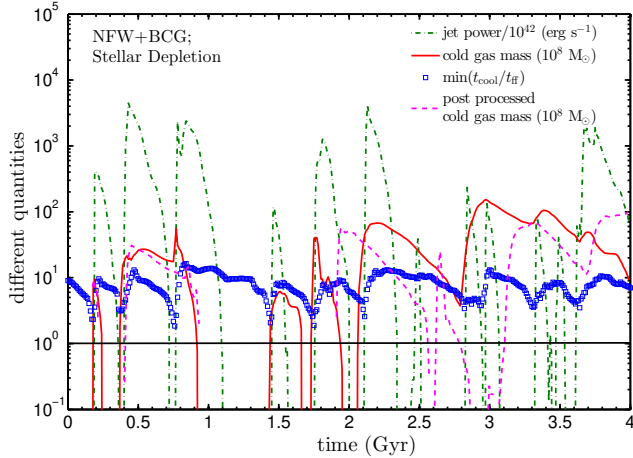


FIG. 5.— Jet power (dot-dashed green line), cold gas mass (solid red line) and $\min(t_{\text{cool}}/t_{\text{ff}})$ (blue squares) for the NFW+BCG run with stellar gas depletion. The magenta dashed line shows the post processed (using Eq. 10 in Prasad et al. 2015) cold gas mass with $\tau = 200$ Myr for the NFW+BCG run without stellar depletion. Jet power and $\min(t_{\text{cool}}/t_{\text{ff}})$ show similar values to the NFW+BCG run without stellar depletion, but the time duration between consecutive jet events is shorter. The total cold gas at the end of 4 Gyr is an order of magnitude smaller in comparison to the NFW+BCG without stellar gas depletion (see the right panel of Fig. 4). Note that the lowest $\min(t_{\text{cool}}/t_{\text{ff}})$ is always above 2, like in the NFW+BCG case without stellar gas depletion.

3.2. Effects of Stellar Gas Depletion

One of the problems with recent hydrodynamic simulations of AGN feedback in galaxy clusters is the formation of a massive torus in the central few kpc of the cluster core (Gaspari et al. 2012; Li et al. 2015; Prasad et al. 2015), which is generally on the higher end of the ob-

served cold gas mass spectrum (this of course depends on the choice of ϵ). The cold gas in the torus is dominated by rotation and is decoupled from the feedback cycle. However, observations show that only a few clusters like Hydra (Hamer et al. 2014) have rotating cold disks extending few kpc. In most clusters no such prominent structure is observed and most of the cold gas is in extended filaments (Russell et al. 2016, 2017). To ameliorate the problem of excess cold gas mass in our simulations, we include a simplified model for the depletion of cold gas due to star formation as described in section 2.3.

For the NFW+BCG run with stellar gas depletion (labeled NFW+BCGd) the mass flow rate across the inner boundary is $7.1 M_\odot \text{ yr}^{-1}$, comparable to that in the run without depletion (see Table 1). This means that star formation primarily affects the rotationally dominant cold gas component (torus) while the radially dominant component with a free-fall time shorter than the depletion time (τ ; see Eq. 3), which controls the feedback cycle, remains largely unaffected.

Figure 5 shows the evolution of jet power, cold gas mass and $\min(t_{\text{cool}}/t_{\text{ff}})$ for the NFW+BCGd run. The dashed magenta line shows the total cold gas mass when cold gas is depleted in post processing (as in Prasad et al. 2016) for the NFW+BCG run, while the solid red line shows the total cold gas mass for the NFW+BCGd run. In both cases, the cold gas depletion time, τ , is 200 Myr. Both approaches show the dynamic nature of the amount of cold gas, with the peak cold gas mass at $\approx 10^{10} M_\odot$. This is unlike the run without cold gas depletion in which the total cold gas mass gets saturated after 2 Gyr at $\gtrsim 10^{10} M_\odot$ (see the right panel of Fig. 4). With stellar depletion, the total cold gas in the core lies in the range

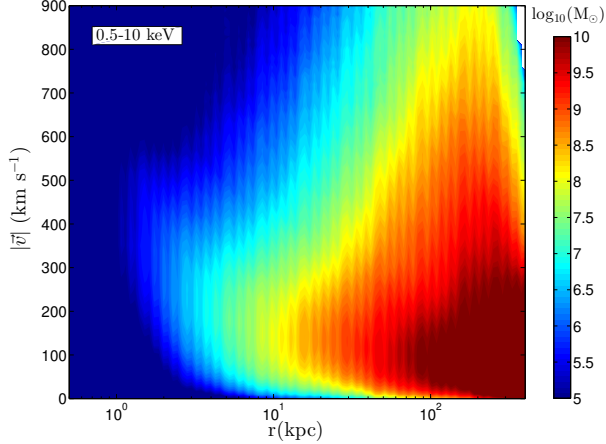


FIG. 6.— Time-averaged (from 1-4 Gyr) velocity-radius distribution of the X-ray gas (0.5-10 keV) for the NFW+BCG run without stellar depletion. The plot shows the $|\mathbf{v}| - r$ mass distribution - $d^2M/(d\ln|\mathbf{v}|d\ln r)$ ($\Delta v = 10 \text{ km s}^{-1}$, $\Delta \log_{10} r = 0.03$ are the bin sizes). In the central regions ($r < 60 \text{ kpc}$), most of the hot gas mass (of the order of $10^{10} M_{\odot}$) is in the velocity range of 0-400 km s^{-1} . However, small amount of gas ($\sim 10^7 M_{\odot}$) has velocity going up to 1000 km s^{-1} . A similar velocity-radius map of the X-ray gas is obtained for the NFW+BCG run with stellar depletion.

of observed cold gas mass in cool cluster cores (see Figure 8 in Prasad et al. 2016).

The evolution of jet power with time for the NFW+BCGd run in Figure 5 shows significant difference from the NFW+BCG run in Figure 4. While the peak jet power is roughly of the same order for the two runs, the duration of each jet event is smaller in the run with stellar gas depletion. When cold gas gets depleted because of star formation, AGN jets encounter less resistance (cold clumps help energy deposition in the core by inducing local turbulence; c.f. Fig. 8) on their way out from the cluster core. As a result, they deposit most of their energy at larger distances. Cluster core is not overheated despite a large jet power, and the cluster core maintains its cool characteristics for longer. This leads to frequent jet events of shorter intervals.

The evolution of $\min(t_{\text{cool}}/t_{\text{ff}})$ ratio with time for the run with stellar gas depletion in Figure 5 is as expected. Right before a major jet event, this ratio dips below 10 signaling a cooling phase in the cluster core. The cooling phase is followed by a strong accretion phase which gives rise to a powerful jet outburst. This heats up the core, pushing $\min(t_{\text{cool}}/t_{\text{ff}})$ above 10, marking the completion of one cooling-heating cycle. This is repeated multiple times during our simulation. The $\min(t_{\text{cool}}/t_{\text{ff}})$ ratio fluctuates between 2-20 during the course of the simulation, with 77% of the time it lying below 10 but only 19% of the time below 5. Like the NFW+BCG run with no depletion, even here the $\min(t_{\text{cool}}/t_{\text{ff}})$ ratio never drops below 2.

3.3. Turbulence in Cool-Core Clusters

AGN-ICM interaction gives rise to turbulent motion of the gas in the ICM. In our previous paper (Prasad et al. 2015), we looked at the cold gas kinematics in the cluster core due to AGN-ICM interaction. Here, we look at the motion of X-ray emitting hot gas (0.5-10 keV) in the cluster core and compare it with the *Hitomi* results for

the Perseus cluster (Hitomi Collaboration et al. 2016).

Figure 6 shows the average (from 1-4 Gyr) velocity-radius distribution ($d^2M/d\ln|\mathbf{v}|d\ln r$) of the X-ray gas (0.5 - 10 keV) for the NFW+BCG run. The central 100 kpc hot gas distribution shows that most of the hot gas mass ($\gtrsim 10^{10} M_{\odot}$) lies in the velocity range of 0-400 km s^{-1} . For 100-300 kpc radial range, the hot gas velocity has a broader distribution with the velocity range expanding to 0-500 km s^{-1} . There is also a small fraction of gas with velocity reaching beyond 900 km s^{-1} . The small fraction of gas attains this high value due to AGN jets. Beyond 300 kpc, most of the mass has velocity in the range of 0-200 km s^{-1} .

The left panel of Figure 7 shows line of sight velocity dispersion (LOSVD) with time within 30-60 kpc of the cluster center for the X-ray gas in our NFW+BCG run. We show the results for all X-ray gas (0.5-10 keV) and for 2-8 keV plasma in the same spherical shell. The latter range corresponds to the gas responsible for *Fe XXV* 6.6 keV line probed by *Hitomi* in the core of Perseus cluster.

The LOSVD is calculated for the velocity component parallel to the y-axis (perpendicular to jet injection direction; $\theta = 90^\circ$) and z-axis (parallel to jet injection direction; $\theta = 0^\circ$). Other than a slight divergence in the LOSVD of the X-ray gas at late times ($t > 3 \text{ Gyr}$) for $\theta = 90^\circ$, the results for the hot and total X-ray gas, and between different orientations are very similar. The timing of the sharp rise and fall in the velocity dispersion correlates with the rise in jet power (see the right panel of Fig. 4). The AGN jet outbursts push the LOSVD from 100 km s^{-1} range to $\sim 250 \text{ km s}^{-1}$. As the jet activity dies down, velocity dispersion drops back to the 100 km s^{-1} level. The LOSVD is in the same range as earlier independent simulations (Li et al. 2016; Lau et al. 2017). The $\theta = 90^\circ$ LOSVD is higher in the quiescent state for 0.5-10 keV compared to 2-8 keV because of a large fraction of infalling/rotating soft X-ray emitting gas ($< 2 \text{ keV}$) in the mid-plane at these epochs.

The right panel of Figure 7 shows the probability distribution function (PDF) of the line of sight velocity (LOSVD) perpendicular to the jet direction ($\theta = 90^\circ$) for the hot X-ray gas (2-8 keV) within 30-60 kpc (to compare with *Hitomi* observations of the Perseus core). The solid black line shows the time-averaged PDF (averaged from 1-4 Gyr), and dashed red and dot-dashed blue lines show the PDF at 2.35 Gyr and 2.1 Gyr. These times correspond to a trough and a peak, respectively, in the LOSVD plot in the left panel. The PDF for the LOSVD peaks close to 0 km s^{-1} , showing the absence of significant bulk flows in the hot phase. During strong AGN jet activity, the PDF of the LOSVD has an extended high velocity ($\gtrsim 300 \text{ km s}^{-1}$) tail which is absent otherwise. LOSVD distribution is similar along the jet direction ($\theta = 0^\circ$), except with somewhat higher velocity tails when the jet is active.

3.4. Spread Of Metals By AGN Jets

AGN jets help transport the metals from star forming core regions (and also metals produced by type Ia supernovae in the BCG) in cool core clusters. Here we use a simplified model of metal transport in which all metals are injected close to the center in the jet injection region. Our model should be fine to quantify metal transport in cool-core clusters due to AGN jets.

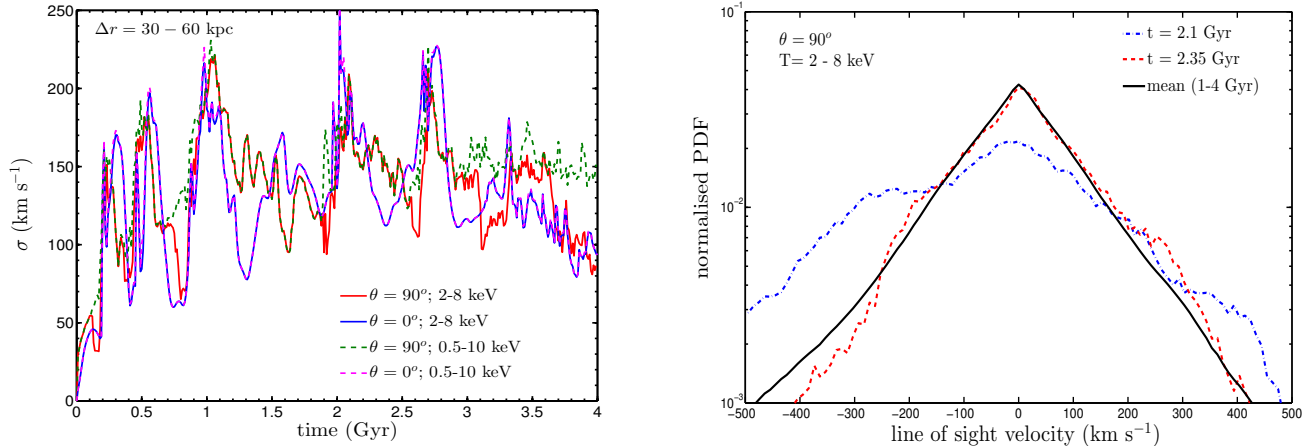


FIG. 7.— Left panel shows the line of sight velocity dispersion (LOSVD) with time for 2-8 keV plasma (a proxy for Fe XV line emission) and total X-ray gas (0.5-10 keV) within 30-60 kpc of the NFW+BCG run without stellar gas depletion. The solid lines (blue line is parallel to jet direction (z-axis) while red line is perpendicular to jet direction) represent the LOSVD for 2-8 keV gas. Dashed lines (green line is perpendicular to the jet direction while magenta line is parallel to the jet direction) show the LOSVD for the total X-ray gas (0.5-10 keV). Right panel shows the probability distribution function (PDF) of the volume-weighted line of sight velocity perpendicular to the jet direction for the 2-8 keV gas. The solid black line is the time-averaged PDF between 1-4 Gyr, while the dashed red and dot-dashed blue lines correspond to the PDF at $t = 2.35$ Gyr and $t = 2.1$ Gyr, respectively. These times correspond to a trough and a peak in the LOSVD as seen in the left panel. Note the presence (absence) of high velocity tails at 2.1 (2.35) Gyr.

Figure 8 shows the extent of metal distribution due to AGN jets in the NFW+BCG simulations, at the end of 4 Gyr for the runs with (left panel) and without (right panel) stellar depletion. These plots show that AGN jets can spread metals beyond 400 kpc in both cases, predominantly in the jet direction. There is a noticeable difference between metallicity distribution at larger radii in the runs with and without gas depletion. Jets encounter less resistance due to clumpy cold clouds in the simulation with cold gas depletion and therefore travel mostly along the direction of jet injection without much dispersion in the transverse directions. Without stellar depletion the metal distribution is much more laterally extended at large radii because of vorticity generation at the hot-cold interface of the cold gas clouds (see the upper panel of Figure 8).

Figure 9 shows the angular distribution of mass weighted metallicity (Eq. 6) of the ICM for different radial shells ($\Delta r = 20$ kpc) at 4 Gyr for the NFW+BCG runs with and without stellar gas depletion. The distribution shows bimodality with metallicity peaking near the polar regions, as expected from Figure 8. However, the metallicity peak is higher by a factor of 2 for smaller radii with stellar depletion as compared to the run without stellar depletion, again reflecting higher lateral mixing in the latter case.

Figure 10 shows the angle-averaged distribution of metals as a function of radius at 4 Gyr (Eq. 5) for the NFW+BCG runs without stellar gas depletion. Metallicity shows a steep rise in the cluster core ($r < 0.02r_{500}$), while beyond $0.02r_{500}$ there is only $\lesssim 2\times$ change in metallicity over the background $0.3Z_\odot$. This shows that the impact of AGN jets in distributing the metals is limited to the cluster core. The shaded regions depict the 1σ scatter of metallicity about the mean (cyan is for O, grey is for Fe) as a function of radius for the sample of clusters and groups in Mernier et al. 2017. The observations show a more extended metal distribution (till $0.1r_{500}$) as compared to our simulations.

4. DISCUSSION

Recent observations of galaxy clusters have thrown up many challenges for the simulations of cold mode feedback in cool cores. Two of the key challenges are: (i) the near absence of cores with $\min(t_{\text{cool}}/t_{\text{ff}}) < 10$ (Hogan et al. 2017a,b; see however, Voit & Donahue 2015; Lakhchaura et al. 2016; Pulido et al. 2018), unlike smaller ratios (down to unity) seen in simulations (albeit for a short time); and (ii) the absence of massive rotating cold tori in observations, which are routinely seen within the central few kpc of cool core simulations, except in Hydra A (Hamer et al. 2014). In light of these discrepancies, we have incorporated two effects in our simulations to see if simulations can be reconciled with observations: (i) a central BCG potential; and (ii) a simple model for gas depletion due to star formation. We study the effects of these new physical ingredients on the long term evolution of cluster cores. Additionally, we quantify other important X-ray observables such as metallicity and level of turbulence in the X-ray emitting gas in cool cluster cores.

4.1. How much below 10 does $\min(t_{\text{cool}}/t_{\text{ff}})$ fall?

Pinning the gravitational acceleration to that of the central BCG at small radii, Hogan et al. 2017a,b argue that almost none of the cool cluster cores go below the $\min(t_{\text{cool}}/t_{\text{ff}}) = 10$ threshold for the presence of cold gas motivated by simulations. While Hogan et al. (2017b) use a sample of 33 H α line emitting galaxy clusters and find one core with $\min(t_{\text{cool}}/t_{\text{ff}})$ slightly below 10 (they quote a range in $\min[t_{\text{cool}}/t_{\text{ff}}]$ of 10-35), more recent observations of 23 cool cores with confirmed detections of CO-emitting gas (Pulido et al. 2018) find 5 systems below 10 (although still above 7). In this sample 10 out of 23 CO-emitting cool cores have $\min(t_{\text{cool}}/t_{\text{ff}})$ between 8-12 and one system below 8. Further, the latest observations of the 40 low mass halos (galaxies) by Babyk et al. (2018) show that $\min(t_{\text{cool}}/t_{\text{ff}})$ falls to as low as 5. In this sample 8 out of 40 systems have

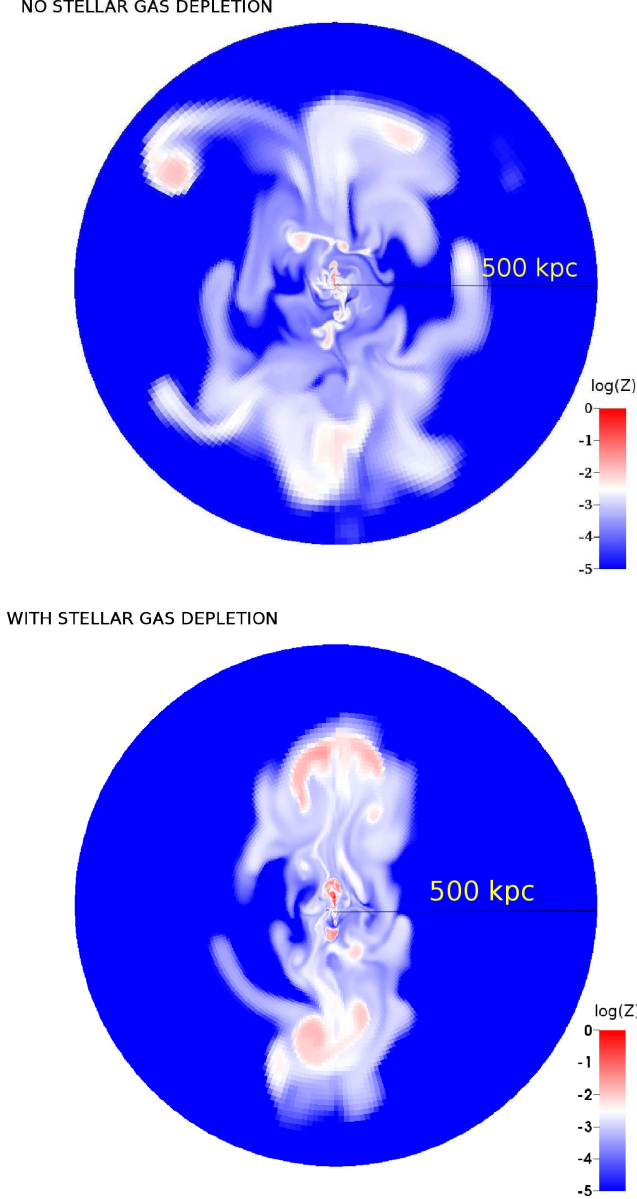


FIG. 8.— Metallicity at 4 Gyr for the NFW+BCG runs with (bottom panel) and without (top panel) stellar gas depletion. Note that the lateral mixing of metals is more extensive in absence of gas depletion.

$\min(t_{\text{cool}}/t_{\text{ff}}) \leq 10$. Voit & Donahue (2015), using a singular isothermal sphere model (with a fixed velocity dispersion of 250 km s^{-1}) for the BCG potential, found a $\min(t_{\text{cool}}/t_{\text{ff}})$ ratio in the range 5–20 for cool core clusters. Following the method of Voit & Donahue (2015), O’Sullivan et al. (2017) find that out of five galaxy groups with jets, four have $\min(t_{\text{cool}}/t_{\text{ff}}) < 15$ with lowest value at 7.4. Thus, the disagreement between cool-core observations and simulations highlighted in Hogan et al. (2017b) does not appear to be serious.

The one noticeable discrepancy is the presence of snapshots in which $\min(t_{\text{cool}}/t_{\text{ff}})$ falls as low as 1 for the NFW run (see the left panel of Fig. 4). However, the BCG potential somewhat alleviates this problem by shortening the feedback response time (as t_{ff} in the core

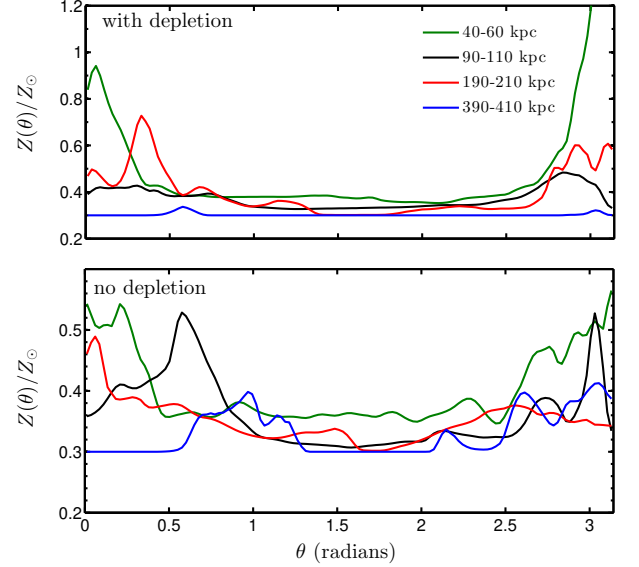


FIG. 9.— Angular spread of metals due to AGN jets at 4 Gyr (see Eq. 6) for shells at different radii ($\Delta r = 20 \text{ kpc}$) for the NFW+BCG runs without (lower panel) and with (upper panel) stellar depletion. The peaks at $\theta = 0$ and π show that jets are unable to disseminate metals in the equatorial regions to large radii. The metallicity peaks in the polar regions are higher at smaller radii in the run with stellar gas depletion as compared to the run without depletion. A metallicity floor of $0.3Z_{\odot}$ is added to these profiles.

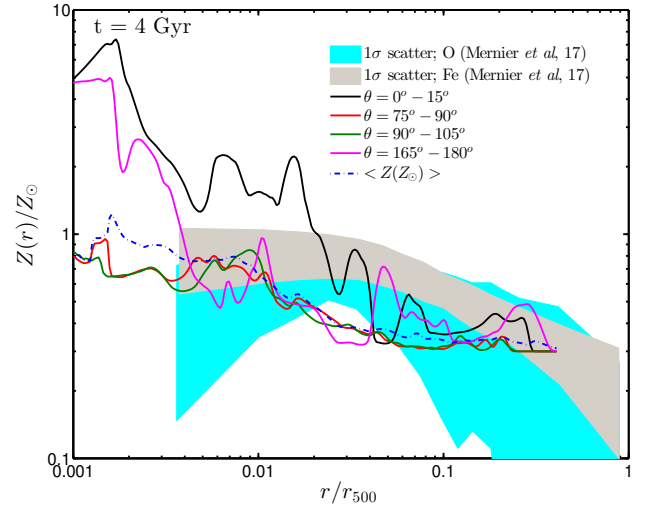


FIG. 10.— Angle-averaged metallicity profile (dot-dashed blue line) at 4 Gyr for the NFW+BCG run without stellar gas depletion. In the core ($r < 0.02r_{500}$) metallicity rises sharply above the background metallicity of $0.3Z_{\odot}$ while beyond $0.02r_{500}$ AGN jets seem to have no impact on the metallicity. The grey shaded region is the 1σ spread about the mean for Fe and the cyan shaded region is 1σ spread about the mean for O as a function of radius for the full sample (cluster+groups) in Mernier et al. (2017). Observations show that the metallicity is elevated for much larger radii ($r < 0.1r_{500}$) in clusters in comparison to our simulation. Solid lines show the metallicity profiles within 15° parallel and perpendicular to the jet direction. The average metallicity profile closely follows the equatorial profiles because of a larger solid angle. A metallicity floor of $0.3Z_{\odot}$ is added to these profiles.

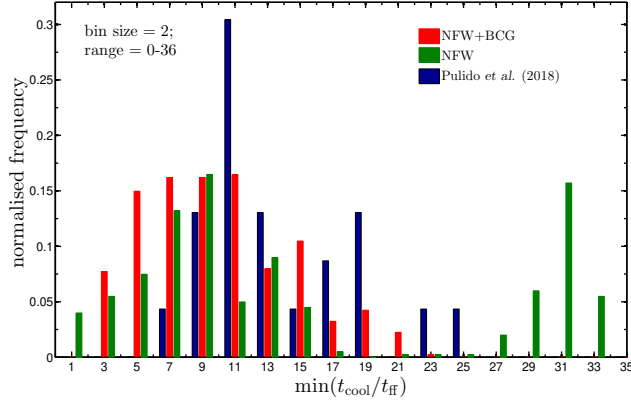


FIG. 11.— The normalized histograms for the distribution of simulated clusters (see Table 1) and observed cluster cores that show CO emission (Pulido et al. 2018) as a function of $\min(t_{\text{cool}}/t_{\text{ff}})$. Notice that the simulated NFW distribution is bimodal and $\min(t_{\text{cool}}/t_{\text{ff}})$ goes to as low as unity in this case. All simulated clusters are biased toward lower $\min(t_{\text{cool}}/t_{\text{ff}})$ compared to observations for our choice of ϵ .

is shorter) and preventing the core from cooling below $\min(t_{\text{cool}}/t_{\text{ff}}) = 2$. In this case feedback acts fast and feedback jet heating cycle starts before the core can cool too much. Moreover, for the same reason, the jet power and $\min(t_{\text{cool}}/t_{\text{ff}})$ after the jet event do not increase to large values.

Figure 11 shows the histograms of $\min(t_{\text{cool}}/t_{\text{ff}})$ for our NFW and NFW+BCG runs and from the cool core sample of Pulido et al. (2018) of the clusters with CO detection. Clearly the NFW simulation shows occurrence of clusters with $\min(t_{\text{cool}}/t_{\text{ff}})$ as low as unity. Moreover, the NFW core distribution is bimodal with another peak in $\min(t_{\text{cool}}/t_{\text{ff}})$ occurring at ≈ 30 . Similar results are obtained for 3-D NFW cluster simulations in Prasad et al. (2015), which uses a smaller value of feedback efficiency (ϵ). With the inclusion of BCG there are no cores with $\min(t_{\text{cool}}/t_{\text{ff}}) < 2$ and there is no second peak in $\min(t_{\text{cool}}/t_{\text{ff}})$ distribution. While the latter inference depends on ϵ , the former is a generic feature of a deeper potential well. Thus the inclusion of a BCG potential brings the simulations in a closer agreement with cool core observations but even then the observed distribution is shifted toward higher $\min(t_{\text{cool}}/t_{\text{ff}})$. The peak of the observed and simulated BCG distributions is within a factor of two. The disagreement at low values of $\min(t_{\text{cool}}/t_{\text{ff}})$ may be due to several factors: observational biases due to sample selection (e.g., even different samples by the same group show different distributions of $\min[t_{\text{cool}}/t_{\text{ff}}]$; e.g., compare Hogan et al. 2017b; Pulido et al. 2018; Babyk et al. 2018); low spatial resolution (see Fig. 8 in Hogan et al. 2017b) and breakdown of spherical symmetry in the core where $\min(t_{\text{cool}}/t_{\text{ff}})$ occurs; simulations do not include important physical effects such as thermal conduction and stellar feedback that can increase $\min(t_{\text{cool}}/t_{\text{ff}})$.

Now we discuss the issue of the occurrence of cold gas even when $\min(t_{\text{cool}}/t_{\text{ff}}) > 10$. Early idealized thermal instability models with heating balancing average cooling in radial shells (McCourt et al. 2012; Sharma et al. 2012; Choudhury & Sharma 2016) for the hydrostatic ICM confined by NFW gravity showed $\min(t_{\text{cool}}/t_{\text{ff}}) \lesssim 10$ to be a necessary condition for cold gas condensation. Amount

and extent of cold gas condensation is higher for a smaller $\min(t_{\text{cool}}/t_{\text{ff}})$. In these models without angular momentum, extra gas from the core drops out leaving behind a core with $\min(t_{\text{cool}}/t_{\text{ff}}) \gtrsim 10$ (the exact value of this threshold depends on the $t_{\text{cool}}/t_{\text{ff}}$ profile, as investigated in Choudhury & Sharma 2016) that is no longer susceptible to multiphase condensation.

The more realistic feedback AGN jet-ICM simulations show irregular cooling and heating cycles of the core, with $\min(t_{\text{cool}}/t_{\text{ff}})$ falling below 10 in the cooling phase and rising above the threshold value after the cold-gas-driven AGN jet overheats the core to $\min(t_{\text{cool}}/t_{\text{ff}}) \gtrsim 10$. The fraction of time the core spends with $\min(t_{\text{cool}}/t_{\text{ff}}) > 10$ depends on the halo mass and the feedback efficiency. For a higher feedback efficiency and a shallower gravitational potential, the core spends a longer time in an over-heated state with $\min(t_{\text{cool}}/t_{\text{ff}}) > 10$. E.g., Table 1 shows that the NFW run with a shallower potential spends a shorter time with $\min(t_{\text{cool}}/t_{\text{ff}}) \lesssim 10$ as compared to the NFW+BCG runs, for the same feedback efficiency. Unlike in idealized thermal instability simulations (and 2-D axisymmetric jet-ICM simulations), angular momentum of cold gas plays a crucial role in 3-D simulations. The core can retain substantial amount of cold gas even in the heating phase as the cold gas supported by angular momentum is not quickly dispersed or converted into stars. Thus, in realistic 3-D jet-ICM simulations the correlation between various cool-core diagnostics is not strong (e.g., see Fig. 10 in Li et al. 2015 and Fig. 14 in Prasad et al. 2015). For example, Figures 4 & 5 show that substantial cold gas (and consequently star formation) is present even if $\min(t_{\text{cool}}/t_{\text{ff}})$ is in the range 10-30 and not necessarily < 10 , consistent with the observations.

4.2. Turbulence in Cool Cores

Indirect constraints on turbulent velocities – based on surface brightness fluctuations (e.g., Zhuravleva et al. 2014), scattering of resonant lines (e.g., Werner et al. 2009), comparison of optical and X-ray derived gravitational accelerations (e.g., Churazov et al. 2008) – in cool cluster cores show that the turbulent energy is $\lesssim 10\%$ of the thermal energy. X-ray line spectra from RGS (Reflection Grating Spectrometer) on XMM-NEWTON, because of its insufficient spectral resolution, could only put weak upper limits on non-thermal velocities (Sanders et al. 2011). The situation improved after the soft X-ray spectrometer (SXS) on *Hitomi*, with its superior spectral resolution, directly measured the line of sight turbulent velocity dispersion $\approx 164 \pm 10 \text{ km s}^{-1}$ within 30-60 kpc of the Perseus core (Hitomi Collaboration et al. 2016). The turbulent pressure is only $\sim 4\%$ of the thermal pressure, despite a fairly large jet/cavity power $\sim 10^{45} \text{ erg s}^{-1}$ (Birzan et al. 2004; see Fig. 4 for comparison).

Equating turbulent heating rate density ($\rho u_L^3/2L$; u_L is the velocity measured at scale L) and radiative cooling rate density ($n_e n_i \Lambda$; $n_{e/i}$ is electron/ion number density and Λ is the cooling function), we obtain that a turbulent velocity of

$$u_L \approx 450 \text{ km s}^{-1} (L_{30} \Lambda_{-23} n_{e,0.05})^{1/3} \quad (7)$$

is required for turbulent heating to balance radiative cooling losses, where L_{30} is the driving length scaled to 30 kpc, Λ_{-23} is the cooling function scaled to 10^{-23} erg

$\text{cm}^3 \text{s}^{-1}$ and n_e is electron number density scaled to 0.05 cm^{-3} . This is much larger than the 3-D velocity dispersion measured in the core of Perseus $\approx \sqrt{3} \times 164 = 285 \text{ km s}^{-1}$. Moreover, for cold gas condensation not to be suppressed by turbulent mixing, condensation should occur at scales larger than the driving scale (see section 4.1 in Banerjee & Sharma 2014). While *Hitomi* observations rule out turbulent heating with a driving scale $\gtrsim 10 \text{ kpc}$ as the dominant heating mechanism in the core, turbulent mixing of the core and the hot outskirts and/or AGN bubble is still possible (e.g., Banerjee & Sharma 2014; Hillel & Soker 2016; Yang & Reynolds 2016a).

We have quantified turbulent velocities in the hot gas in our simulations that broadly agree with observations. Figure 6 shows the velocity-radius distribution of the hot gas (0.5-10 keV) mass and shows that most of the X-ray emitting gas has 3-D turbulent velocity $\lesssim 500 \text{ km s}^{-1}$. Figure 7 shows the 1-D line of sight velocity dispersion in the core as a function of time (left panel) and the pdf of the LOS velocity (right panel). The turbulent velocity increases with a rise in jet power, but only up to $\lesssim 200 \text{ km s}^{-1}$. The velocity dispersion in the direction of the jet is slightly higher than in the perpendicular direction and the turbulent velocity even in the quiescent state is $\gtrsim 80 \text{ km s}^{-1}$. A weak turbulent velocity motivates other models such as intermittent shocks (e.g., Li et al. 2017) and turbulent mixing (e.g., Banerjee & Sharma 2014; Hillel & Soker 2017) as the agents responsible for heating of the cool core.

4.3. Metal Distribution in Cool Cores

Observations show that the outskirts ($r > r_{2500}$, the radius within which the mean matter density is 2500 times the critical density of the universe; for our choice of parameters, $r_{2500} = 0.25r_{200} = 459 \text{ kpc}$) of galaxy clusters have roughly isotropic distribution of metals (Tamura et al. 2004; Fujita et al. 2008; Simionescu et al. 2011; Werner et al. 2013), which is close to 0.3 times the solar metallicity across different systems. Moreover, the cool-core clusters have a rising metallicity toward the center (De Grandi & Molendi 2001; Leccardi & Molendi 2008; Ettori et al. 2015). While AGN jets play a key role in metal transport in the central regions of cool core clusters, our simulations show that they cannot be responsible for the isotropic distribution of metals in cluster outskirts (see Fig. 8). Metal enrichment during the galaxy assembly stage at redshifts $\gtrsim 1$ and mixing driven by mergers seem responsible for such an isotropic and universal metal distribution in the cluster outskirts. The observed large-scale metal enrichment of galaxy clusters sheds light on the cluster formation environment at higher redshifts.

Further, a quantitative comparison of our metal distribution with the observed metallicity shows that our metal distribution due to AGN jets is too narrowly distributed toward the center (see Fig. 10). This finding is similar to Kannan et al. (2017), who compare metal transport with and without thermal conduction in cosmological simulations of galaxy clusters including AGN feedback. In absence of thermal conduction, like us, they find a very centrally peaked metallicity distribution. With thermal conduction mixing is more efficient, and metals and heat are spread out more uniformly and

to larger radii (see Fig. 3 in Kannan et al. 2017 and Fig. 1 in Sharma et al. 2009b). Thus the shallow metallicity profiles of cool core clusters compared to our simulations (see Fig. 10) point to the importance of (anisotropic) thermal conduction in heat and metal transport in cluster cores. An additional caveat is that our idealized simulations do not include cosmological halo mergers that can further stir the ICM, especially at higher redshifts (e.g., see Vogelsberger et al. 2018).

5. CONCLUSIONS

We study the effects of the gravity of the brightest central galaxy (BCG) and depletion of cold gas due to star formation in our simulations to compare with the observations of cool core clusters. We also study the nature of turbulence in cool cluster cores and the metal distribution due to AGN jets. Following are our key conclusions:

1. The presence of BCG potential does not have an impact on the temperature in the cluster core. However, for a fixed feedback efficiency the presence of the BCG increases the average density of hot gas in the core. A larger core density decreases the core entropy and the $t_{\text{cool}}/t_{\text{ff}}$ ratio, on average (see Fig. 2). AGN jets cause greater disruption in the core of the shallower NFW potential as compared to the NFW+BCG potential. A stronger gravity due to the central BCG makes the feedback jets respond faster and prevents $\min(t_{\text{cool}}/t_{\text{ff}})$ from falling below 2, discernibly higher than the minimum value with only the NFW potential (≈ 1). For the same reason the jet power with the inclusion of the BCG potential does not rise beyond $10^{46} \text{ erg s}^{-1}$. The $\min(t_{\text{cool}}/t_{\text{ff}})$ distribution of our BCG simulations is still biased toward smaller values compared to the observations (Fig. 11), but the discrepancy is at less than a factor of two level. Moreover, 3-D jet simulations produce cold gas with angular momentum which can exist even with $\min(t_{\text{cool}}/t_{\text{ff}})$ as high as 30, in agreement with observations. Given a dispersion in the observational results and the low angular resolution in the core, the discrepancy between observations and realistic 3-D feedback jet simulations is not glaring.
2. Star formation, modeled with a gas depletion time of 0.2 Gyr, removes the cold gas present in the clumps and torus in the cluster core. This brings down the cold gas mass within the observed range (see Fig. 5). Moreover, the outgoing AGN jets encounter less resistance with the depletion of cold gas, and the transfer of heat from AGN jets to the entire cluster core is less efficient (see Fig. 8). This results in more frequent AGN jet events with stellar depletion.
3. The line of sight velocity dispersion of X-ray gas in the cluster core shows that the turbulence due to AGN jets is not strong enough for turbulent heating to balance radiative cooling in cluster cores. We find the 1-D velocity dispersion to be in the range of $80\text{--}250 \text{ km s}^{-1}$, consistent with recent observations of the Perseus cluster by *Hitomi* (see Fig.

- 6). The turbulent velocity is larger when AGN jet is active, and the line of sight velocity dispersion is slightly larger along the jet direction rather than perpendicular to this direction during the active jet phase (see Fig. 7).
4. Gas depletion due to star formation also modulates the anisotropic metal distribution in galaxy clusters due to AGN jets as outflowing metal-rich gas faces less hindrance from the cold gas clouds. Metals are able to travel unhindered for the most part to outer radii and so the metal distribution is mostly confined in the jet direction. Moreover, the observed metal distribution in our simulations is too sharply peaked toward the center as compared to the observations of cool cores (see Fig. 10). Thermal conduction (both isotropic and anisotropic) can help spread heat and metals more

uniformly and farther out by overcoming strong entropy stratification. This may bring the metallicity distribution in line with the observations.

This work is partly supported by India-Israel joint research grant (6-10/2014[IC]). DP is supported by a CSIR grant (09/079[2599]/2013-EMR-I) and IISc RA fellowship. AB acknowledges funding from NSERC Canada through the Discovery Grant program, the Institut Lagrange de Paris, and Pauli centre for Theoretical Studies ETH UZH. He also thanks the Institut d'Astrophysique de Paris (IAP), at the Institute for Computational Sciences and University of Zurich for hosting him. We acknowledge the support of the Supercomputing Education and Research Centre (SERC) at IISc for facilitating our use of Cray XC40-SaharaT cluster on which our simulations were carried out. DP wants to thank Naveen Yadav for useful suggestions.

REFERENCES

- Babuk, I. V., McNamara, B. R., Nulsen, P. E. J., et al. 2018, ArXiv e-prints, arXiv:1802.02589
- Banerjee, N., & Sharma, P. 2014, MNRAS, 443, 687
- Birzan, L., Rafferty, D. A., McNamara, B. R., Wise, M. W., & Nulsen, P. E. J. 2004, ApJ, 607, 800
- Choudhury, P. P., & Sharma, P. 2016, MNRAS, 457, 2554
- Churazov, E., Forman, W., Vikhlinin, A., et al. 2008, MNRAS, 388, 1062
- Cielo, S., Babul, A., Antonuccio-Delogu, V., Silk, J., & Volonteri, M. 2018, ArXiv e-prints, arXiv:1801.04276
- De Grandi, S., & Molendi, S. 2001, ApJ, 551, 153
- Ettori, S., Baldi, A., Balestra, I., et al. 2015, A&A, 578, A46
- Fabian, A. C., Sanders, J. S., Allen, S. W., et al. 2003, MNRAS, 344, L43
- Fujita, Y., Tawa, N., Hayashida, K., et al. 2008, PASJ, 60, S343
- Gaspari, M., Ruszkowski, M., & Oh, S. P. 2013, MNRAS, 432, 3401
- Gaspari, M., Ruszkowski, M., & Sharma, P. 2012, ApJ, 746, 94
- Guo, F., & Oh, S. P. 2008, MNRAS, 384, 251
- Hamer, S. L., Edge, A. C., Swinbank, A. M., et al. 2014, MNRAS, 437, 862
- Hillel, S., & Soker, N. 2016, MNRAS, 455, 2139
- . 2017, MNRAS, 466, L39
- Hitomi Collaboration, Aharonian, F., Akamatsu, H., et al. 2016, Nature, 535, 117
- Hogan, M. T., McNamara, B. R., Pulido, F., et al. 2017a, ApJ, 837, 51
- . 2017b, ArXiv e-prints, arXiv:1704.00011
- Kannan, R., Vogelsberger, M., Pfrommer, C., et al. 2017, ApJ, 837, L18
- Kirkpatrick, C. C., Gitti, M., Cavagnolo, K. W., et al. 2009, ApJL, 707, L69
- Lakhchaura, K., Saini, T. D., & Sharma, P. 2016, MNRAS, 460, 2625
- Lau, E. T., Gaspari, M., Nagai, D., & Coppi, P. 2017, ApJ, 849, 54
- Leccardi, A., & Molendi, S. 2008, A&A, 487, 461
- Li, Y., Bryan, G. L., Ruszkowski, M., et al. 2015, ApJ, 811, 73
- Li, Y., Ruszkowski, M., & Bryan, G. L. 2016, ArXiv e-prints, arXiv:1611.05455
- . 2017, ApJ, 847, 106
- McCourt, M., Sharma, P., Quataert, E., & Parrish, I. J. 2012, MNRAS, 419, 3319
- McDonald, M., Veilleux, S., Rupke, D. S. N., & Mushotzky, R. 2010, ApJ, 721, 1262
- McNamara, B. R., Nulsen, P. E. J., Wise, M. W., et al. 2005, Nature, 433, 45
- Mernier, F., de Plaa, J., Kaastra, J. S., et al. 2017, A&A, 603, A80
- Mignone, A., Bodo, G., Massaglia, S., et al. 2007, ApJS, 170, 228
- Mittal, R., Whelan, J. T., & Combes, F. 2015, MNRAS, 450, 2564
- Navarro, J. F., Frenk, C. S., & White, S. D. M. 1997, ApJ, 490, 493
- O'Sullivan, E., Giacintucci, S., David, L. P., Vrtilek, J. M., & Raychaudhury, S. 2011, MNRAS, 411, 1833
- O'Sullivan, E., Ponman, T. J., Kolokythas, K., et al. 2017, MNRAS, 472, 1482
- Pizzolato, F., & Soker, N. 2005, ApJ, 632, 821
- Pope, E. C. D., Babul, A., Pavlovski, G., Bower, R. G., & Dotter, A. 2010, MNRAS, 406, 2023
- Prasad, D., Sharma, P., & Babul, A. 2015, ApJ, 811, 108
- . 2016, ArXiv e-prints, arXiv:1611.02710
- Pulido, F. A., McNamara, B. R., Edge, A. C., et al. 2018, ApJ, 853, 177
- Rafferty, D. A., McNamara, B. R., Nulsen, P. E. J., & Wise, M. W. 2006, ApJ, 652, 216
- Revaz, Y., Combes, F., & Salomé, P. 2008, A&A, 477, L33
- Russell, H. R., McNamara, B. R., Fabian, A. C., et al. 2016, MNRAS, 458, 3134
- Russell, H. R., McDonald, M., McNamara, B. R., et al. 2017, ApJ, 836, 130
- Sanders, J. S., Fabian, A. C., & Smith, R. K. 2011, MNRAS, 410, 1797
- Sharma, P., Chandran, B. D. G., Quataert, E., & Parrish, I. J. 2009a, ApJ, 699, 348
- Sharma, P., Chandran, B. D. G., Quataert, E., & Parrish, I. J. 2009b, in American Institute of Physics Conference Series, Vol. 1201, American Institute of Physics Conference Series, ed. S. Heinz & E. Wilcots, 363–370
- Sharma, P., McCourt, M., Quataert, E., & Parrish, I. J. 2012, MNRAS, 420, 3174
- Simionescu, A., Werner, N., Böhringer, H., et al. 2009, A&A, 493, 409
- Simionescu, A., Allen, S. W., Mantz, A., et al. 2011, Science, 331, 1576
- Sun, M. 2009, ApJ, 704, 1586
- Tamura, T., Kaastra, J. S., den Herder, J. W. A., Bleeker, J. A. M., & Peterson, J. R. 2004, A&A, 420, 135
- Vogelsberger, M., Marinacci, F., Torrey, P., et al. 2018, MNRAS, 474, 2073
- Voigt, L. M., & Fabian, A. C. 2004, MNRAS, 347, 1130
- Voit, G. M., & Donahue, M. 2015, ApJL, 799, L1
- Voit, G. M., Donahue, M., Bryan, G. L., & McDonald, M. 2015, Nature, 519, 203
- Werner, N., Urban, O., Simionescu, A., & Allen, S. W. 2013, Nature, 502, 656
- Werner, N., Zhuravleva, I., Churazov, E., et al. 2009, MNRAS, 398, 23
- Yang, H.-Y. K., & Reynolds, C. S. 2016a, ApJ, 829, 90
- . 2016b, ApJ, 818, 181

Zhuravleva, I., Churazov, E., Schekochihin, A. A., et al. 2014,
Nature, 515, 85